Influence of point defects on the near edge structure of hexagonal boron nitride

Nicholas L. McDougall,[1,*] Jim G. Partridge,[1] Rebecca J. Nicholls,[2] Salvy P. Russo,[3] and Dougal G. McCulloch[1]

[1]*Physics, School of Sciences, RMIT University, GPO Box 2476V, Melbourne, Victoria, 3001, Australia*
[2]*Department of Materials, University of Oxford, Parks Rd, Oxford, Oxfordshire, OX1 3PH, United Kingdom*
[3]*ARC Centre of Excellence in Exciton Science, Physics, School of Science, RMIT University, Melbourne, Australia*

Hexagonal boron nitride (hBN) is a wide-band-gap semiconductor with applications including gate insulation layers in graphene transistors, far-ultraviolet light emitting devices and as hydrogen storage media. Due to its complex microstructure, defects in hBN are challenging to identify. Here, we combine x-ray absorption near edge structure (XANES) spectroscopy with *ab initio* theoretical modeling to identify energetically favorable defects. Following annealing of hBN samples in vacuum and oxygen, the B and N K edges exhibited angular-dependent peak modifications consistent with in-plane defects. Theoretical calculations showed that the energetically favorable defects all produce signature features in XANES. Comparing these calculations with experiments, the principle defects were attributed to substitutional oxygen at the nitrogen site, substitutional carbon at the boron site, and hydrogen passivated boron vacancies. Hydrogen passivation of defects was found to significantly affect the formation energies, electronic states, and XANES. In the B K edge, multiple peaks above the major $1s$ to π^* peak occur as a result of these defects and the hydrogen passivated boron vacancy produces the frequently observed doublet in the $1s$ to σ^* transition. While the N K edge is less sensitive to defects, features attributable to substitutional C at the B site were observed. This defect was also calculated to have mid-gap states in its band structure that may be responsible for the 4.1-eV ultraviolet emission frequently observed from this material.

I. INTRODUCTION

Boron nitride (BN) has two main crystalline phases: cubic BN (cBN) and hexagonal BN (hBN). Possessing a graphite-like structure, hBN consists of strong B-N covalent bonds forming sp^2 bonded hexagons, with weak bonding between planes. Electrons in the B-N bonds are more confined to the N atoms due to their higher electronegativity, leading to some ionicity and a wide band gap [1]. hBN is a prospective material for use in far-ultraviolet light emitting devices [2], paired with graphene for transistor applications [3], and as a hydrogen storage medium [4]. However, for these applications to develop, the effect structural defects have on the properties of hBN must be understood.

Defects significantly influence the electrical, optical, and magnetic properties of hBN. For example, the luminescence spectra contain features within the band gap attributed to stacking faults [5] and impurities [6,7], including single photon emission believed to result from point defects [8]. O plasma treatment has increased the conductivity of hBN through the introduction of vacancy or substitutional defects [9], and magnetic centers have been measured in powder samples, believed to result from N vacancies or C impurities [10,11]. Given these observations, precise identification of defects is vital. Scanning probe microscopy has revealed that point defects are common in hBN, but has not enabled accurate classification [12,13]. Secondary ion mass spectrometry has revealed high C and O content, particularly near the surface of cBN and hBN crystals [14], however, does not distinguish bonding. Transmission electron microscopy (TEM) has permitted B vacancies (V_B) and N vacancies (V_N) to be differentiated, yet beam damage is often coincident [15,16]. Despite calculations showing that V_N

is more stable than V_B [17,18], the latter is more prevalent in electron irradiated samples due to the lower knock-on energy of B [19]. TEM has also revealed impurities may be in the form of substitutional defects such as C dimers and O substituting at the N site (O_N) [20,21]. C substitution can occur in TEM due to residual hydrocarbons in the sample/instrument which migrates under the action of the electron beam [22], limiting the study of intrinsic defects. While microscopy has enabled defects in hBN to be investigated, complementary methods are required to provide element specific bonding information.

X-ray absorption spectroscopy (XAS) provides bonding and structural information sensitive to perturbations caused by defects [23]. The near edge structure superimposed on each XAS core loss edge, known as x-ray absorption near edge structure (XANES), probes the unoccupied density of states local to the absorbing atom. This technique is also complementary to electron energy loss spectroscopy (EELS) performed in TEM. Previous studies of hBN have shown that the 1s to π^* transition in the B K edge consists of a single peak at ~192 eV [24,25]. Additional peaks in its vicinity are often observed in hBN materials and attributed to defects. Two of these peaks have been assigned to B-B bonding [26] and B-O bonding [27] due to peak alignments with metallic boron and boron oxide references. The remaining two have either been attributed to single or multiple N vacancies [25,28], O substituted at one or more N sites [29,30], interactions between transition metal substrates [31], or magnetic polarons resulting from displaced B atoms [32]. The N K edge is also sensitive to defects with a pre-edge feature being attributed to interstitial N [25,28], or transition metal substrate interactions [31]. In summary, debate remains over the origin of many of the spectral features produced by hBN.

Hydrogen is often used in hBN synthesis [33] and has been shown to be readily unintentionally incorporated into the material [34,35]. Furthermore, porous or disordered hBN

---

*Corresponding author: nicholas.mcdougall@rmit.edu.au

have shown potential as hydrogen storage media, exhibiting uptake to 2.6 wt. % [4,36]. Theoretical modeling within the density functional theory (DFT) framework predicts favorable hydrogen absorption on hBN monolayers with C substitutional defects, calculating an increased binding energy in the vicinity of C_B or C_N [37]. Atomic and molecular hydrogen is also calculated to dissociate and preferentially bond at vacancy sites [38]. Despite these observations, the effect hydrogen has on defects in hBN and whether hydrogens' incorporation produces features in XANES is unclear.

Interpretation of XANES is nontrivial and often accurate peak assignments require theoretical modeling. We recently showed that DFT can reproduce the XANES of crystalline cBN [39] and hBN [40], and identified substitutional O defects in electron irradiated cBN [41]. Calculations of XANES have successfully reproduced experimental defect signatures for Si incorporated in cBN [42], distinguished between tri- and quad-coordinated Si in graphene [43], identified the local environment of ion implanted B or N in graphene [44], and reproduced the spectra of various dangling bond arrangements on the edge of a graphene sheet [45,46]. Recent work has also revealed signatures in experiment and in calculations resulting from B-terminated tetravacancies in monolayer hBN [47]. In this work, high-resolution XANES coupled with *in situ* ion irradiation and annealing was used to investigate defects in hBN. Several forms of hBN were studied including single crystals, powders and thin films. We employ *ab initio* theoretical modeling to calculate XANES of various energetically favorable defects and compare these with the experimental observations.

II. METHODOLOGY

XANES were collected at room temperature (RT) from magnetron sputtered BN thin-film samples, single crystal hBN (HQ Graphene, Netherlands) and hBN powder (Goodfellows, England) at the soft x-ray beamline of the Australian Synchrotron. The thin films were deposited from a 99.9% boron target (Testbourne, England) operated at radio frequency with 200-W power. Depositions were performed at 3.0 mTorr in a 17% N_2 in Ar environment at RT and 200 °C, with a −50-V substrate bias. During the XANES measurements, an electron flood gun was employed to minimize sample charging. The spectra were collected using the partial electron yield from a horizontally polarized x-ray beam incident at angles of 20°, 55°, and 90° from the surface (55° shown unless otherwise specified) and from as-prepared and treated samples. Ar^+ irradiation treatments were performed on the hBN powder sample using 2.0-kV ions and irradiated for 20 minutes. Annealing was performed for 1 hour in a connected chamber at 600 °C, at a pressure of 5×10^{-6} Torr and subsequently in 20% O_2 in Ar gas at 400 °C and 600 Torr. Spectra were normalized between the pre- and postedges (unless otherwise specified) using the XAS software package ATHENA [48]. Images and selected area diffraction patterns were acquired from hBN powder and cross-sectioned thin-film samples using a JEOL 2100F TEM operating at an accelerating voltage of 200 kV.

Ab initio electronic structure calculations were performed using CASTEP [49]. Six point defects were considered: the B

vacancy (V_B), N vacancy (V_N), C substituted for B (C_B), C substituted for N (C_N), O substituted for B (O_B), and O substituted for N (O_N). Each defect was considered as nonpassivated and as passivated with one or three H atoms to saturate any dangling bonds. Multiple extended substitutional O defects were also considered: O substituted at two neighboring N sites ($2O_N$) and O substituted at three neighboring N sites ($3O_N$). In all calculations, the local spin density approximation was used to treat exchange and correlation. The electronic wave functions were expanded using plane waves with a 500 eV kinetic energy cutoff and "on-the-fly" generated pseudopotentials were implemented to enable the inclusion of core holes [50]. The electronic states were populated using a 0.1 eV Fermi smearing parameter. All calculations used Monkhorst-Pack k-point Brillouin zone sampling [51] with a maximum k-point spacing of 0.023 Å^{-1} in the a direction and 0.038 Å^{-1} in the c direction. Structures were optimized using the Broyden-Fletcher-Goldfarb-Shanno algorithm until the force on each ion was less than 0.01 eV/Å and the total energy/atom changed by less than 5×10^{-6} eV. The point defect calculations were performed on a 128 atom $4 \times 4 \times 2$ hBN supercell [lattice parameters $a = 9.965$ Å, $c = 12.93$ Å, and space group 194 ($P6_3/mmc$)]. This cell size was found to be sufficient to render core-hole core-hole interactions negligible within hBN. The extended substitutional O calculations were performed on a 200 atom $5 \times 5 \times 2$ hBN supercell [lattice parameters $a = 12.45$ Å, $c = 12.93$ Å, and space group 194 ($P6_3/mmc$)]. Band-structure calculations were performed on pristine hBN and the six point defect structures using a maximum k-point spacing of 0.02 Å^{-1} in a and c directions.

XANES were calculated using the post-processing tool OptaDOS [52], which uses CASTEP's electronic structure calculations to compute absorption spectra. This calculation involves the evaluation of the transition matrix elements between the core states on the absorbing atoms and the unoccupied final states, which are dependent on the density of states (DOS). The core states are obtained from an all-electron calculation and can be modified to include a core-hole. The presence of a core-hole affects both the occupied and unoccupied DOS, including the projected unoccupied DOS used in the XANES calculation. The absorption process in XANES follows the dipole approximation, in which only angular momentum quantum number l changes of ± 1 contribute to the spectra. Instrumental- and lifetime-broadening effects are also included in OptaDOS. A 0.8 eV adaptive broadening scheme was applied to the DOS calculation [53]. Gaussian instrumental broadening of 0.3 eV (0.5 eV) was included in the calculated B (N) K edges along with an energy dependent Lorentzian lifetime component of 0.1 eV. In all calculations, a $1s$ electron was removed from the target excited atom (to create a core-hole) and a neutralizing charge was applied to the system. The spectra from defective hBN were normalized and aligned to the extended fine structure in the calculated spectra from pristine hBN.

The formation energies E^f of point defects were calculated using [54]

$$E^f[X] = E_{\text{tot}}[X] - E_{\text{tot}}[\text{bulk}] - \sum n_i \mu_i, \quad (1)$$
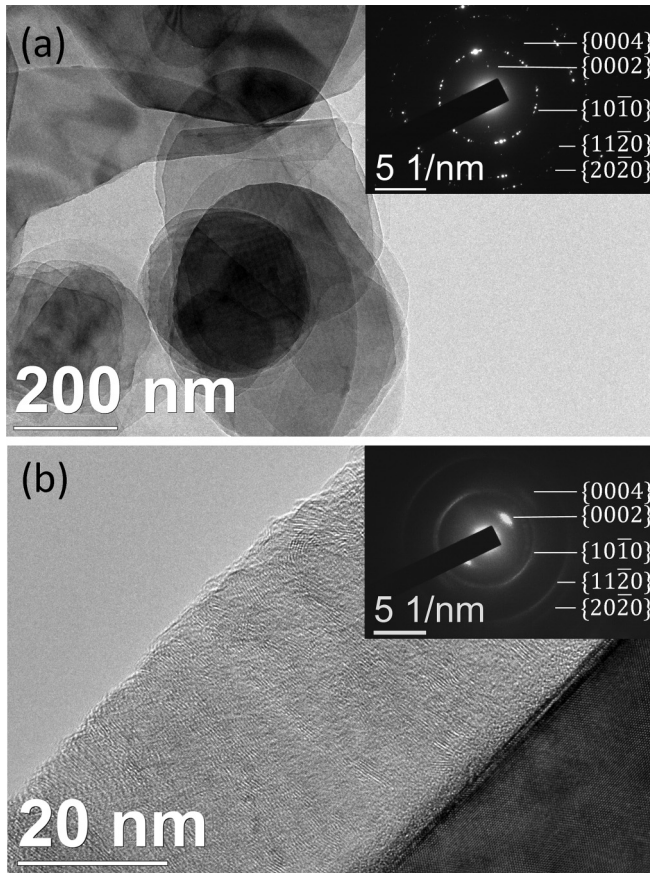
FIG. 1. TEM images and inset diffraction patterns of (a) hBN powder showing overlapping platelets with some folding of the layers and (b) a cross-sectioned turbostratic hBN thin film with a preferred crystallographic orientation normal to the substrate (bottom right of image).

where $E_{tot}[X]$ is the total energy of the supercell with neutral defect X and E_{tot}[bulk] is the total energy of the nondefective bulk supercell. n_i is the number of atoms of element i that are added ($n_i > 0$) or removed ($n_i < 0$) from the host structure. μ_i is the chemical potential of element i. The chemical potential of H, N, O were computed from the gas phase, C from CH_4 and B from α-rhombohedral B [lattice parameters $a = c = 4.98$ Å and space group 166 (*R-3M*)].

III. RESULTS AND DISCUSSION

Figure 1 shows TEM images and diffraction patterns (inset) from (a) the hBN powder and (b) thin film grown on Si at RT. The hBN powder, consisting of platelets up to 1 μm in diameter, produced a diffraction pattern that was indexed to hBN [inset Fig. 1(a)]. Some of the platelets were partially folded. The thin film in Fig. 1(b) exhibits microstructure typical of disordered turbostratic hBN grown with a preferred crystallographic orientation normal to the substrate. The diffraction pattern [inset Fig. 1(b)] was again indexed to hBN and confirmed the preferred orientation in the film. The in-plane lattice parameters determined from the diffraction patterns of the hBN powder and thin film were similar ($a = 2.5$ Å). However, the c-axis lattice parameter
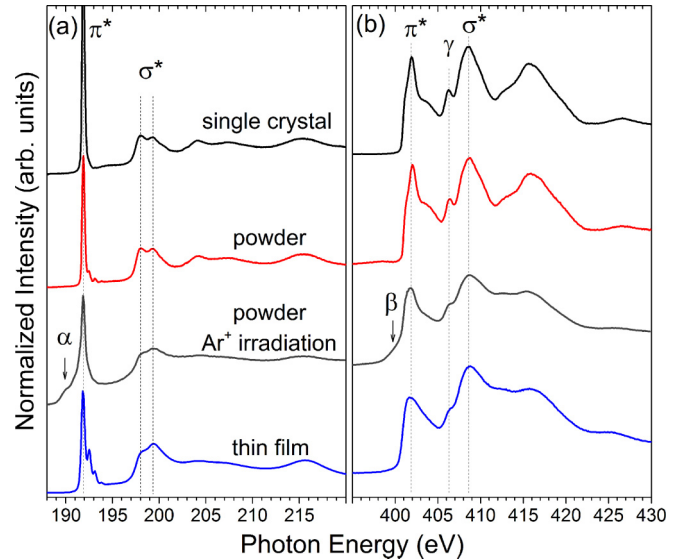

FIG. 2. XANES spectra for the (a) B K edge and (b) N K edge from hBN single crystal, hBN powder, Ar$^+$ irradiated hBN powder, and hBN thin film grown at 200 °C.

differed between samples. In the powder, it was 6.7 Å, as expected for crystalline hBN [33]. In the hBN film, it was on average 7.2 Å, indicative of increased disorder.

Figure 2 shows the XANES from single crystal hBN, hBN powder with and without Ar$^+$ irradiation, and a hBN thin film deposited at 200 °C. The peak labeled π^* at 191.9 eV on the B K edge [Fig. 2(a)] is produced by the transition of 1s electrons to π^* states while the doublet feature (198.0 eV, 199.4 eV) and higher energy peaks are produced mainly by transitions to σ^* states [24]. Three additional peaks in the vicinity of the principle π^* peak (most evident in the thin-film B K edge) have previously been attributed to defects [28–32]. These peaks are not resolved in the XANES from the least defective hBN single crystal. Irradiation of the powder leads to broadening of the π^* peak and a pronounced shoulder (labeled α) on its lower energy side. This peak has been attributed to metallic B [26], formed following ion bombardment. Significant differences in the ratio of peak intensities for the σ^* doublet feature are evident between samples. Although the σ^* doublet feature is routinely observed in bulk, monolayer and nanotube hBN samples, there is debate over its origin [24,31,55].

In the case of the N K edge [Fig. 2(b)], the peak at 401.8 eV is attributed to 1s to π^* transitions, while a shoulder at 406.4 eV (labeled γ) and the 408.7-eV peak and above are mainly due to 1s to σ^* transitions. The single crystal and powder samples produce identical N K edge spectra, despite the observed differences in the B K edge. This implies the N K edge is less sensitive to changes to the local environment. Irradiation of the hBN powder results in broadening of features and a lower energy shoulder at ~400 eV (labeled β). This feature has previously been attributed to interstitial N [25,28], which is likely formed post ion bombardment. The N K edge for the thin-film sample is comparable to that of the irradiated powder, indicating a similar environment about the N atoms for both. Broadening and energy downshift of the N K edge π^* peak
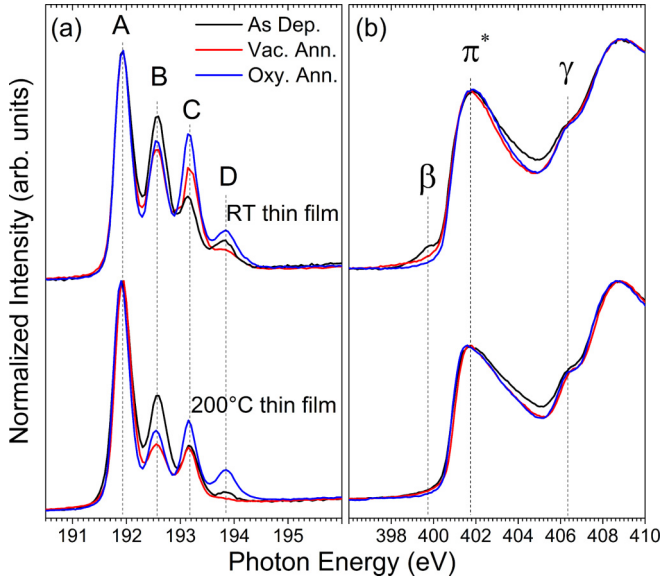
FIG. 3. (a) B K edge and (b) N K edge XANES of as-deposited, vacuum annealed and oxygen annealed hBN thin films grown at RT and 200 °C. The spectra are normalized to the first π^* peak (labeled A in the B K edge).

FIG. 4. Angular dependence of B K edge XANES for the 200 °C thin-film sample. Spectra are normalized to the first π^* peak (labeled A). Inset shows peaks A–D over a reduced energy range following background subtraction.

has been observed for BN nanotubes [27] and is attributed to disorder induced curvature in the BN layers [see Fig. 1(b) and inset].

Figure 3(a) shows the effect of annealing, in vacuum and oxygen on the B K edge XANES from two thin-film samples, deposited at RT and 200 °C. Significant changes only occurred in the vicinity of the $1s$ to π^* peak, which consists of four peaks labeled A–D at 191.9, 192.6, 193.2, and 193.8 eV. Peak A corresponds to the $1s$ to π^* transitions discussed above. Following annealing in vacuum, the intensities of peaks B and D decrease, and then increase with subsequent annealing in oxygen. This implies some oxygen association. The behavior of peak C is more complex. An increase is observed following both annealing in vacuum and in oxygen for the more disordered RT film, while an increase is only observed following annealing in oxygen for the 200 °C film. Peak C has previously been attributed to O substituted at two N sites ($2O_N$) [29,30]. However, an increase in the intensity of peak C following vacuum annealing appears to contradict this assignment. Figure 4 shows the dependence of the B K edge on the angle of x-ray incidence. There is a significant change in the ratio of the π^* peak A to the σ^* peaks as a function of x-ray incidence angle, indicative of layered structures [23]. The ratios between peak A and peaks B–D do not change with incidence angle (shown more clearly in the background subtracted inset), this indicates that peaks B–D originate from in-plane defects. These results suggest that peak B is associated with substitutional O, which are removed by annealing in a vacuum and created by annealing in oxygen. Peak D is reduced during vacuum annealing and increased during annealing in oxygen, consistent with it being associated with boron oxide, as previously reported [27]. However, our results show that boron oxide is oriented in-plane, contrary to Ref. [29]. The N K edges [Fig. 3(b)] are less sensitive to annealing. However, in the RT film, a pre-edge feature at 399.7 eV (labeled β)
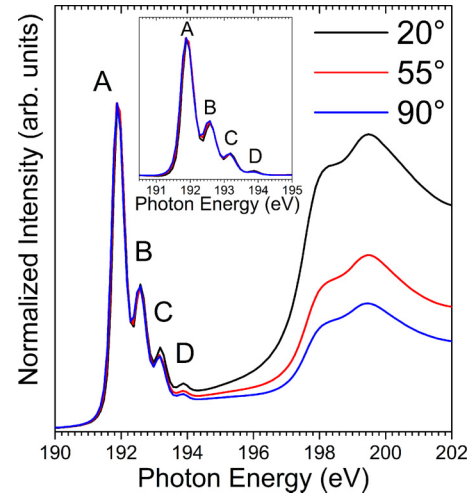
vanishes after annealing in a vacuum and is unaffected by annealing in oxygen. Previously, the origin of this feature has been reported to be interstitial nitrogen [25,28], which may recombine at defect sites or outgas during annealing.

The formation energies of selected defect structures, calculated using the *ab initio* code CASTEP, are compared in Table I. The most favorable nonpassivated point vacancy is the V_N, in agreement with previous work [17,18]. The formation energies of the point vacancies are lowered after C and O substitution, showing that vacancy filling is energetically favorable. The C_B defect has lower formation energy than C_N, in agreement with [56], and the O_N lower than O_B. O_N is calculated to be the most favorable substitutional defect, implying any V_N would fill with O if available. As reported in numerous experiments [7,14,36], O contamination is difficult to eliminate, and is likely responsible for some of the additional features observed in the experimental XANES. Also shown in Table I are the formation energies of defect structures containing two or three O atoms substituting N sites: $2O_N$ and $3O_N$, respectively. As discussed above, peaks C and D in the B K edge [Fig. 3(a)] have previously been attributed to these defects, however both

TABLE I. Formation energies of hBN defects structures with and without H passivation.

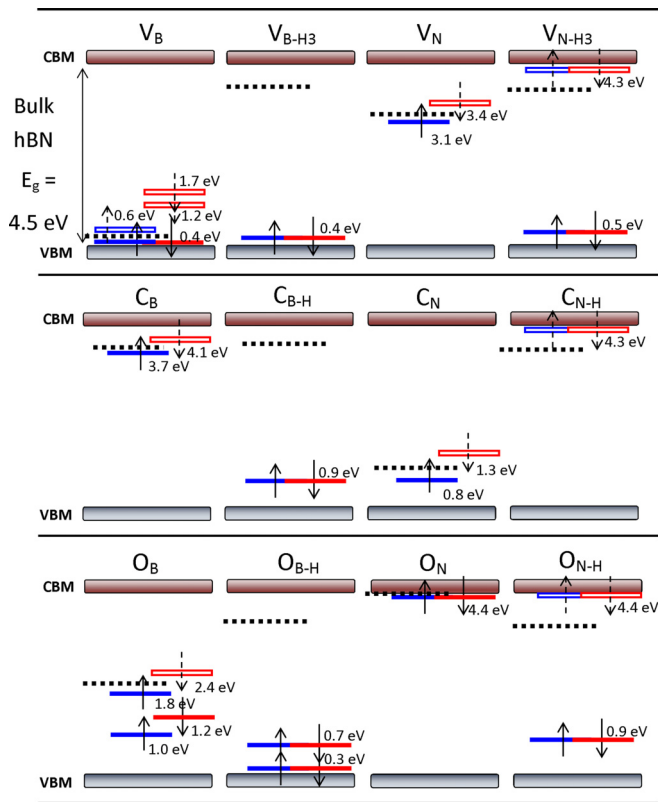| Defect	Formation energy (eV)	
	Nonpassivated	H passivated
V_B	13.1	4.69
V_N	9.85	8.51
C_B	5.59	4.54
C_N	7.86	5.41
O_B	5.19	8.10
O_N	2.20	3.47
$2O_N$	5.08	
$3O_N$	9.55	

FIG. 5. Simplified band-structure diagrams of hBN defect structures at the Γ point. Energy levels are shown relative to the valence-band maximum (VBM) and conduction-band minimum (CBM) of the pristine calculation. Spin up/down states are shown in blue/red. Occupied states are represented by solid rectangles and arrows. Unoccupied states are represented by hollow rectangles and dashed arrows. The Fermi energy levels calculated by CASTEP are shown as dotted lines.

are energetically unfavorable compared with O_N. Since H has been found experimentally in hBN [34,35], the formation energies of H-passivated defects are also shown in Table I. Vacancy defects were passivated with one to three H atoms to saturate dangling bonds. We find passivation by three H atoms to be most favorable. Substitutional defects were passivated with one H atom. H passivation lowers the energy of the point vacancies and of the substitutional C defects, but increases the formation energies of both substitutional O defects. In particular, the formation energy of the V_B is significantly lowered as a result of H passivation (V_{B-H3}), stabilizing this defect and increasing its likelihood to be observed experimentally.

Simplified band-structure diagrams for the point defects considered are shown in Fig. 5 at the Γ point. The Fermi energies calculated by CASTEP are shown as dotted lines. The calculated band gap at the Γ point for pristine hBN was found to be ~4.5 eV. This is consistent with other theoretical works [17,57], but lower than that measured experimentally (~6 eV [7]), due to the known underestimation of the band gap inherent in the DFT method. All nonpassivated defects introduce levels within this band gap, with energies similar to those reported previously for monolayer hBN [57]. V_B

shows three unoccupied and one occupied levels with the latter thought to lead to metallic character [17]. C_B, C_N, and O_B all have nondegenerate states within the gap indicating that these defects may exhibit magnetism [58]. O_N introduces a double degenerate occupied state close to the conduction-band minimum (CBM), which could lead to metallic character [58], and may explain the increased conductivity for oxygen plasma treated hBN samples [9]. H passivation significantly alters the band structure of all defect types. In most cases, H passivation removes the splitting of spin up and spin down states. V_{B-H3} and V_{N-H3} exhibit states either close to the valence band maximum (VBM) or the CBM, resulting in a similar effective band gap to pristine hBN. H passivation of the C and O substitutional defects causes significant changes in the levels of the states within the band gap. Sub-band-gap emission (4.1 eV) is often observed in hBN [6,7], and appears to correlate with C or O impurities [14] in the form of point defects [8]. Our results show that several of the substitutional defects give rise to energy levels within the band gap, consistent with the observed emission.

Figure 6 shows the geometry optimized structures of nonpassivated and H-passivated vacancy defects and their calculated XANES spectra. For the nonpassivated V_B defect, Jahn-Teller distortions reconstruct the vacancy site, breaking the threefold symmetry slightly from D_{3h} to C_{2v}, as calculated by [57,59]. The V_N defect is found to maintain the D_{3h} threefold symmetry. In both defects, the bonds adjoining the vacancies are modified in length. V_B and V_N structures reduce to C_2 and C_s symmetry following H passivation. For the V_{B-H3} structure [Fig. 6(b)], three H atoms passivate the edge N atoms and are oriented above, within and below the hBN plane. In the V_{N-H3} structure [Fig. 6(d)], three H atoms passivate the edge B atoms with one H atom oriented below and two above the plane. The calculated B and N K edge XANES for pristine hBN and vacancy defects are shown in Figs. 6(e) and 6(f) and are compared to experimental XANES from hBN powder. The XANES calculations are symmetry weighted averages of spectra from either the B or N atoms within the shaded regions in Figs. 6(a)–6(d). Spectra from atom sites outside the shaded region resembled that of pristine hBN and were therefore excluded. The pristine hBN calculations reproduce many of the features from the hBN powder, with the exception of the σ^* doublet in the B K edge [Fig. 6(e)] and the lower energy σ^* peak shoulder of the N K edge [Fig. 6(f)]. In our previous work, these additional features were observed in experimental—but not calculated—spectra [40] and were suggested to result from defects not included in the models.

The V_B introduces additional features in the calculated B K edge [Fig. 6(e)]. A pre-edge feature appears at 189.8 eV and the σ^* peak becomes less intense and asymmetric. In the N K edge [Fig. 6(f)], two additional features appear below the π^* peak at 396.4 and 398.2 eV. These pre-edge features arise due to unoccupied acceptor states in the band gap formed from the vacancy (Fig. 5). The lower energy feature below the N K edge π^* peak in the calculated XANES for V_B has been observed experimentally and in calculations by Suenaga et al. [60]. The spectra from the H-passivated V_B (V_{B-H3}) do not exhibit any pre-edge features, consistent with the filling of unoccupied energy levels. In the B K edge, the asymmetric σ^* peak created by V_B becomes a doublet after H passivation (V_{B-H3}).
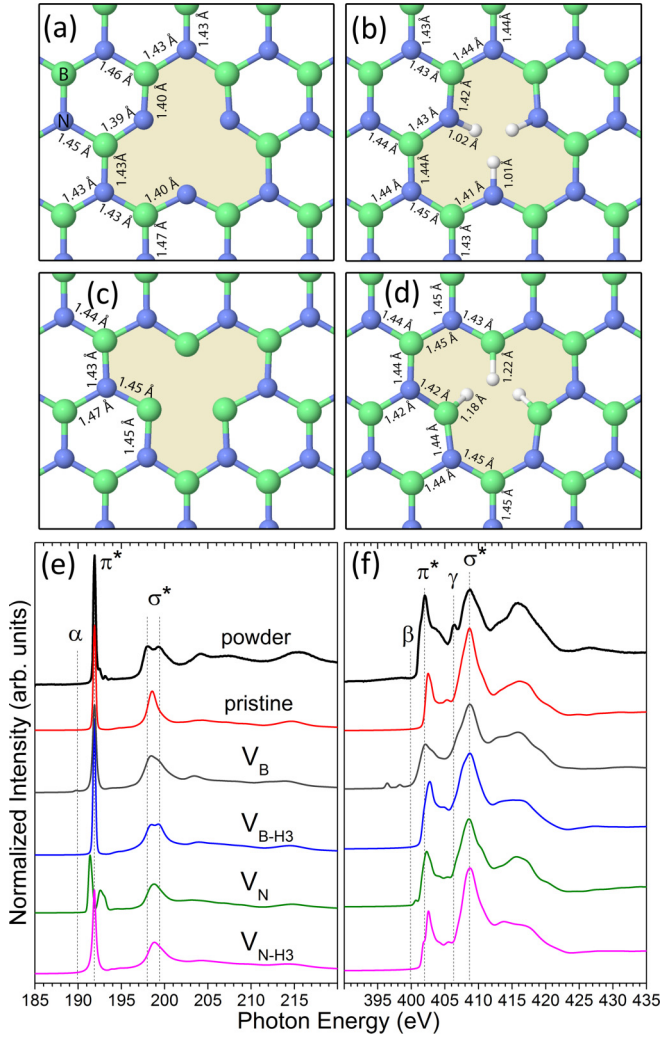
FIG. 6. Structural models of the (a) V_B, (b) V_{B-H3}, (c) V_N, and (d) V_{N-H3} in hBN. The calculated (e) B K edges and (f) N K edges from these defects are compared with pristine hBN and experimental data from hBN powder.

FIG. 7. Structural models of the (a) C_B, (b) C_{B-H}, (c) C_N, and (d) C_{N-H} in hBN. In (b) and (d), the H atoms are above the plane with bond lengths of 1.10 and 1.12 Å to the underlying C. (e) The B K edges and (f) N K edges calculated from these defects are compared with the pristine hBN calculations and experimental data of hBN powder.

The calculated B and N K edges resemble the respective experimental edges, leading us to conclude that V_{B-H3} are common in hBN materials, including high-purity single crystal hBN (Fig. 2). This is consistent with the calculations showing that V_{B-H3} has relatively low formation energy. In the B K edge of the nonpassivated V_N [Fig. 6(e)], additional peaks either side of the pristine π^* peak are observed. These peaks could contribute to the broadened π^* peak measured in the powder following Ar^+ irradiation [Fig. 2(a)], known to create vacancies [61]. Upon H passivation, the spectrum resembles that of pristine hBN as unoccupied acceptor states in the band gap are again filled.

Figures 7(a)–7(d) shows the geometry optimized nonpassivated and H-passivated C substitutional defect structures. C substitution at either a B or N site again modifies the adjoining bond lengths while maintaining the D_{3h} threefold symmetry. Both the H-passivated C_B and C_N structures result in H bound normal to the hBN plane with the C atom displaced towards H, resulting in a sp^3-like puckering with C_{3v} symmetry. Calculations of H bonding on graphene have revealed a similar
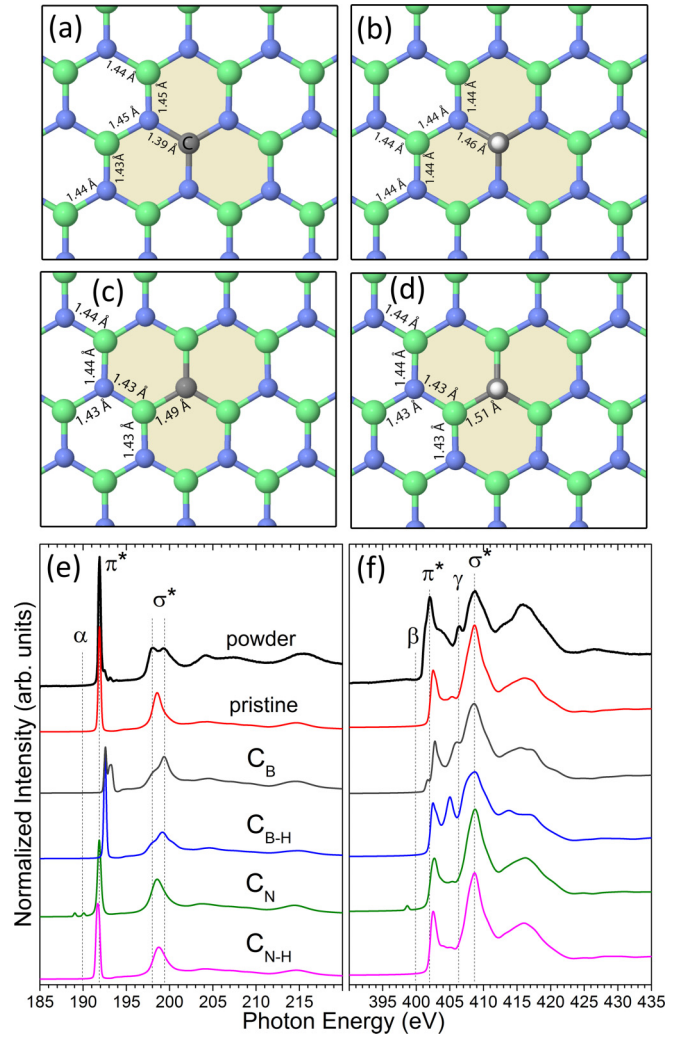
structure [62]. The C_B defect produces distinctly different B and N K edges [Figs. 7(e) and 7(f)] to those from pristine hBN. The π^* peak shifts to a higher energy and is split, while the main σ^* peak has a higher energy and a shoulder. This π^* split feature aligns with that of peaks B and C in the thin-film spectra of Fig. 3(a). The N K edge of C_B has a σ^* feature at 406 eV coinciding with the feature labeled γ observed experimentally from the hBN powder. Of all the defects considered here, only C_B defects replicated this feature. XANES from carbon nitride (CN_x) structures show a lower energy σ^* peak position relative to that of hBN [63], suggesting the γ feature in hBN may relate to C-N bonding. We therefore attribute the 406.4 eV σ^* feature (labeled γ) to C-N bonding present in our samples, either originating from C_B point defects or from larger C inclusions which would have similar C-N bonding at their boundaries [22]. H passivation of C_B (C_{B-H}) results in the B K edge π^* peak shifted to higher energy, without splitting, and the N K edge σ^* shoulder lowered in energy. C_N causes additional
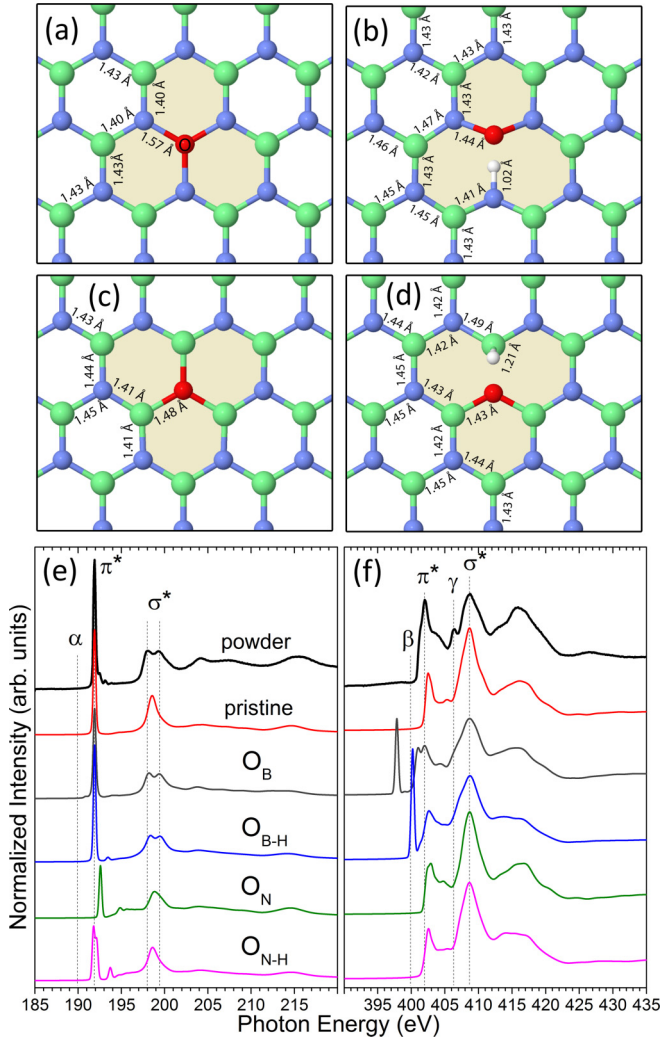
FIG. 8. Structural models of the (a) O_B, (b) O_{B-H}, (c) O_N, and (d) O_{N-H} in hBN. (e) B K edges and (f) N K edges calculated from these defect compared to pristine hBN and experimental data of hBN powder.

pre-edge features in both the B and N K edges, indicating the presence of unoccupied states in the band gap, which are filled upon H passivation (C_{N-H}) (see Fig. 5).

Figures 8(a)–8(d) shows the geometry optimized nonpassivated and H-passivated O substitutional defect structures. The nonpassivated O substitutional defect structures maintain the D_{3h} threefold symmetry. For O_{B-H} and O_{N-H}, H passivation occurs at the neighboring site and not at the substitutional O, reducing the symmetry to C_s for both defects. The O_B and O_{B-H} defects replicate the split in the first σ^* feature ($\sim 198 - 200$ eV) of the B K edge [Fig. 8(e)] from the hBN powder. However, the corresponding N K edges [Fig. 8(f)] do not contain features seen experimentally and we therefore exclude these defects as candidates in hBN. This exclusion is consistent with the high formation energies calculated for O_B and O_{B-H} (Table I) and experimental observations by Krivanek *et al.* [20], where only O_N substitutional defects were observed. O_N, the most energetically favorable defect investigated, causes an upward shift in the π^* peak in the
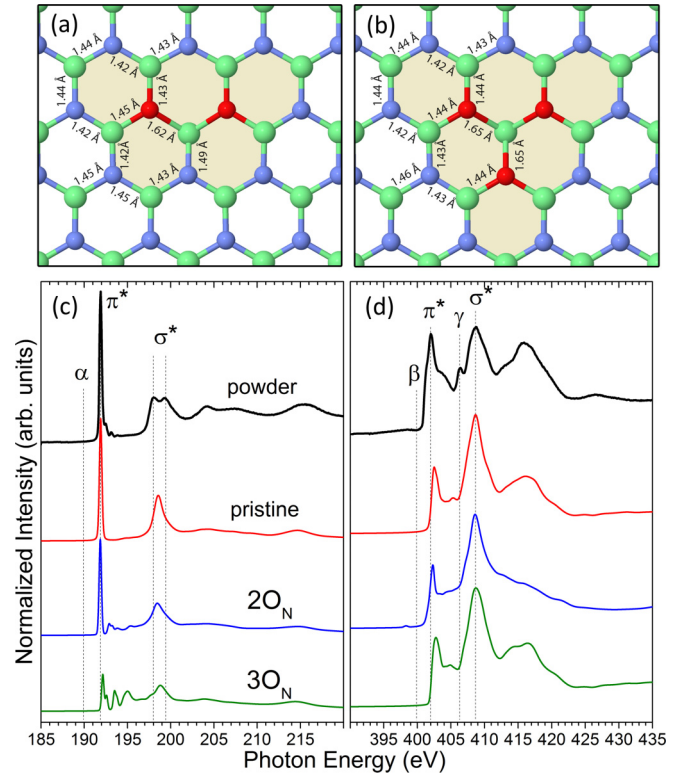

FIG. 9. Structural models of the (a) $2O_N$ and (b) $3O_N$ defects. (c) B K edges and (d) N K edges calculated from multiple O_N substitution defects compared with pristine hBN and experimental data of hBN powder.

B K edge, while the N K edge is similar to that of pristine hBN. The B K edge π^* peak for O_N aligns well with the experimental peak B (Fig. 3), consistent with our annealing experiments, which demonstrated that this peak was O related. We therefore attribute peak B to O_N defects in hBN. O_{N-H} is less energetically favorable than O_N and leads to features in the B K edge not seen experimentally.

Multiple substitutional O defects $2O_N$ and $3O_N$ have been used to explain features C and D in the B K edge (Fig. 3) [29,30]. The geometry optimized $2O_N$ and $3O_N$ defect structures and the corresponding B and N K edges are shown in Fig. 9. For both $2O_N$ and $3O_N$ defects, the central B atom is displaced out of plane, resulting in C_S and C_{3v} symmetry, respectively [Figs. 9(a) and 9(b)]. The calculated formation energies (Table I) of the $2O_N$ and $3O_N$ defects are significantly higher than O_N, implying O clustering is unfavorable. Additionally, our calculated spectra produce multiple features in the B K edge π^* peak region (191–195 eV) that do not correspond with features C and D seen experimentally. Previous work calculating XANES spectra for multiple substitutional O defects constrained the impurities to have double coordination [64]. We have not applied this constraint as experimental observation show triple-coordinated O defects [20].

The B and N K edges from the hBN powder and the 200 °C thin-film sample are compared with calculations from energetically favorable vacancy (V_{B-H3}) and substitutional defects (C_B and O_N) in Fig. 10. The B K edge σ^* doublet
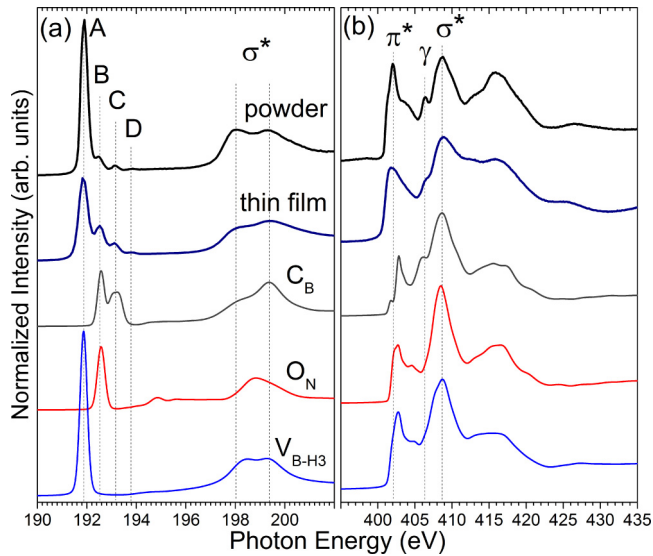
FIG. 10. (a) Calculated B K edges and (b) N K edges from energetically favorable defects compared with experimental edges from hBN powder and the 200 °C thin-film sample.

is well reproduced in the calculated XANES from V_{B-H3} and C_B substitutional defects. The asymmetry in the doublet from the thin-film sample compared to the hBN powder suggests the film has a greater C_B content. In the irradiated hBN powder (Fig. 2), a similar change in the peak ratios within the doublet is observed and attributed to vacancy creation during irradiation, followed by C substitution from the unintentional bombardment of the carbon tape support [29]. The additional 1s to π^* peak at 192.6 eV (peak B) is reproduced by O_N and C_B calculations, and is attributed to O_N. Peak C at 193.2 eV is also consistent with C_B, however, the independent intensity variation in peaks B and C with annealing (Fig. 3) implies multiple contributions, and hence cannot be attributed to C_B alone. In the N K edge, the σ^* peak shoulder at 406.4 eV (labeled γ) is only replicated in the C_B calculation and is attributed to C inclusions forming C-N bonding within hBN.

As discussed above, luminescence studies of hBN often reveal a 4.1 eV sub-band-gap emission. A recent study has shown that single photon emission can occur at this energy [8]. This type of emission in the near UV raises the possibility

that a singlet spin state exists in the excited state, similar to the well-known charged nitrogen vacancy center in diamonds (NV-) [65]. This may be exploitable in applications for which the diamond NV- has been considered. Our results suggest that C_B could be the defect responsible for this emission.

IV. CONCLUSION

We have combined XANES with *ab initio* theoretical modeling to characterize point defects in hBN materials. Effects of annealing and angular dependence on the XANES of hBN signal-crystal, powder, and thin-film samples were assessed. Defect related features in the vicinity of the B K edge π^* peak were found to be in-plane. Theoretical calculations considered H-passivated and nonpassivated point vacancies, C substitutional defects and O substitutional defects. All nonpassivated defects produced levels in the band gap that were largely removed after H passivation. Based on experimental XANES and calculated formation energies, the principle defects in hBN were substitutional O at the N site (O_N), C at the B site (C_B) and H-passivated B vacancies (V_{B-H3}). O_N defects were shown to reproduce the 192.6 eV feature observed experimentally (peak B) in the B K edge. V_{B-H3} defects were calculated to reproduce the σ^* doublet observed experimentally in the B K edge. The lower energy σ^* shoulder in the N K edge is assigned to C-N bonding. Energetically favorable defects all produced signature spectral features enabling their identification using XANES or site-specific electron energy loss spectroscopy. Our results suggest that C_B could be the defect responsible for sub-band-gap emission reported in hBN. This study highlights the significance of hydrogen in boron nitride materials, as formation energies, electronic states and resulting XANES spectra are greatly affected by hydrogen passivation.

[1] Q. H. Weng, X. B. Wang, X. Wang, Y. Bando, and D. Golberg, Chem. Soc. Rev. **45**, 3989 (2016).

[2] K. Watanabe, T. Taniguchi, T. Niiyama, K. Miya, and M. Taniguchi, Nat. Photon. **3**, 591 (2009).

[3] C. R. Dean, A. F. Young, I. Meric, C. Lee, L. Wang, S. Sorgenfrei, K. Watanabe, T. Taniguchi, P. Kim, K. L. Shepard, and J. Hone, Nat. Nanotechnol. **5**, 722 (2010).

[4] P. Wang, S. Orimo, T. Matsushima, H. Fujii, and G. Majer, Appl. Phys. Lett. **80**, 318 (2002).

[5] A. Pierret, J. Loayza, B. Berini, A. Betz, B. Placais, F. Ducastelle, J. Barjon, and A. Loiseau, Phys. Rev. B **89**, 035414 (2014).

[6] L. Museur, E. Feldbach, and A. Kanaev, Phys. Rev. B **78**, 155204 (2008).

[7] K. Watanabe and T. Taniguchi, Int. J. Appl. Ceram. Tec. **8**, 977 (2011).

[8] R. Bourrellier, S. Meuret, A. Tararan, O. Stephan, M. Kociak, L. H. G. Tizei, and A. Zobelli, Nano Lett. **16**, 4317 (2016).

[9] R. S. Singh, R. Y. Tay, W. L. Chow, S. H. Tsang, G. Mallick, and E. H. T. Teo, Appl. Phys. Lett. **104**, 163101 (2014).

[10] A. Katzir, J. T. Suss, A. Zunger, and A. Halperin, Phys. Rev. B **11**, 2370 (1975).

[11] T. Kolodiazhnyi and D. Golberg, Chem. Phys. Lett. **413**, 47 (2005).

[12] D. Wong, J. Velasco, L. Ju, J. Lee, S. Kahn, H. Z. Tsai, C. Germany, T. Taniguchi, K. Watanabe, A. Zettl, F. Wang, and M. F. Crommie, Nat. Nanotechnol. **10**, 949 (2015).

[13] H. Y. Cun, M. Iannuzzi, A. Hemmi, S. Roth, J. Osterwalder, and T. Greber, Nano Lett. **13**, 2098 (2013).

[14] T. Taniguchi and K. Watanabe, J. Cryst. Growth **303**, 525 (2007).

[15] J. C. Meyer, A. Chuvilin, G. Algara-Siller, J. Biskupek, and U. Kaiser, Nano Lett. **9**, 2683 (2009).

[16] C. H. Jin, F. Lin, K. Suenaga, and S. Iijima, Phys. Rev. Lett. **102**, 195505 (2009).

[17] M. S. Si and D. S. Xue, Phys. Rev. B **75**, 193409 (2007).

[18] T. B. Ngwenya, A. M. Ukpong, and N. Chetty, Phys. Rev. B **84**, 245425 (2011).

[19] A. Zobelli, A. Gloter, C. P. Ewels, G. Seifert, and C. Colliex, Phys. Rev. B **75**, 245402 (2007).

[20] O. L. Krivanek, M. F. Chisholm, V. Nicolosi, T. J. Pennycook, G. J. Corbin, N. Dellby, M. F. Murfitt, C. S. Own, Z. S. Szilagyi, M. P. Oxley, S. T. Pantelides, and S. J. Pennycook, Nature **464**, 571 (2010).

[21] C. T. Pan, R. R. Nair, U. Bangert, Q. Ramasse, R. Jalil, R. Zan, C. R. Seabourne, and A. J. Scott, Phys. Rev. B **85**, 045440 (2012).

[22] Z. Liu, L. H. G. Tizei, Y. Sato, Y. C. Lin, C. H. Yeh, P. W. Chiu, M. Terauchi, S. Iijima, and K. Suenaga, Small **12**, 252 (2016).

[23] J. Stöhr, *NEXAFS Spectroscopy 1992* (Springer-Verlag, New York, 1992), p. 3, p. 69

[24] J. B. MacNaughton, A. Moewes, R. G. Wilks, X. T. Zhou, T. K. Sham, T. Taniguchi, K. Watanabe, C. Y. Chan, W. J. Zhang, I. Bello, S. T. Lee, and H. Hofsass, Phys. Rev. B **72**, 195113 (2005).

[25] R. Peter, A. Bozanic, M. Petravic, Y. Chen, L. J. Fan, and Y. W. Yang, J. Appl. Phys. **106**, 083523 (2009).

[26] D. Li, G. M. Bancroft, and M. E. Fleet, J. Electron Spectros. Relat. Phenomena **79**, 71 (1996).

[27] L. J. Liu, T. K. Sham, W. Q. Han, C. Y. Zhi, and Y. Bando, ACS Nano **5**, 631 (2011).

[28] I. Jimenez, A. F. Jankowski, L. J. Terminello, D. G. J. Sutherland, J. A. Carlisle, G. L. Doll, W. M. Tong, D. K. Shuh, and F. J. Himpsel, Phys. Rev. B **55**, 12025 (1997).

[29] I. Caretti and I. Jimenez, J. Appl. Phys. **110**, 023511 (2011).

[30] K. A. Simonov, N. A. Vinogradov, M. L. Ng, A. S. Vinogradov, N. Martensson, and A. B. Preobrajenski, Surf. Sci. **606**, 564 (2012).

[31] A. B. Preobrajenski, A. S. Vinogradov, M. L. Ng, E. Cavar, R. Westerstrom, A. Mikkelsen, E. Lundgren, and N. Martensson, Phys. Rev. B **75**, 245412 (2007).

[32] A. A. Pavlychev, R. Franke, S. Bender, and J. Hormes, J. Phys.: Condens. Matter **10**, 2181 (1998).

[33] A. Pakdel, Y. Bando, and D. Golberg, Chem. Soc. Rev. **43**, 934 (2014).

[34] T. M. Duncan, R. A. Levy, P. K. Gallagher, and M. W. Walsh, J. Appl. Phys. **64**, 2990 (1988).

[35] K. Kim and N. S. Sullivan, Phys. Rev. B **57**, 12595 (1998).

[36] Q. H. Weng, X. B. Wang, C. Y. Zhi, Y. Bando, and D. Golberg, ACS Nano **7**, 1558 (2013).

[37] S. H. Jhi and Y. K. Kwon, Phys. Rev. B **69**, 245407 (2004).

[38] S. A. Shevlin and Z. X. Guo, Phys. Rev. B **76**, 024104 (2007).

[39] D. G. McCulloch, D. W. M. Lau, R. J. Nicholls, and J. M. Perkins, Micron **43**, 43 (2012).

[40] N. L. McDougall, R. J. Nicholls, J. G. Partridge, and D. G. McCulloch, Microsc. Microanal. **20**, 1053 (2014).

[41] N. L. McDougall, J. G. Partridge, D. W. M. Lau, P. Reineck, B. C. Gibson, T. Ohshima, and D. G. McCulloch, MRS Advances **2**, 1545 (2017).

[42] H. Murata, T. Taniguchi, S. Hishita, T. Yamamoto, F. Oba, and I. Tanaka, J. Appl. Phys. **114**, 233502 (2013).

[43] Q. M. Ramasse, C. R. Seabourne, D. M. Kepaptsoglou, R. Zan, U. Bangert, and A. J. Scott, Nano Lett. **13**, 4989 (2013).

[44] D. Kepaptsoglou, T. P. Hardcastle, C. R. Seabourne, U. Bangert, R. Zan, J. A. Amani, H. Hofsass, R. J. Nicholls, R. M. D. Brydson, A. J. Scott, and Q. M. Ramasse, ACS Nano **9**, 11398 (2015).

[45] J. H. Warner, Y. C. Lin, K. He, M. Koshino, and K. Suenaga, Nano Lett. **14**, 6155 (2014).

[46] K. Suenaga and M. Koshino, Nature **468**, 1088 (2010).

[47] O. Cretu, Y. C. Lin, M. Koshino, L. H. G. Tizei, Z. Liu, and K. Suenaga, Phys. Rev. Lett. **114**, 075502 (2015).

[48] B. Ravel and M. Newville, J. Synchrotron Radiat. **12**, 537 (2005).

[49] S. J. Clark, M. D. Segall, C. J. Pickard, P. J. Hasnip, M. J. Probert, K. Refson, and M. C. Payne, Z. Kristallogr. **220**, 567 (2005).

[50] S. P. Gao, C. J. Pickard, A. Perlov, and V. Milman, J. Phys.: Condens. Matter **21**, 104203 (2009).

[51] H. J. Monkhorst and J. D. Pack, Phys. Rev. B **13**, 5188 (1976).

[52] A. J. Morris, R. J. Nicholls, C. J. Pickard, and J. R. Yates, Comput. Phys. Commun. **185**, 1477 (2014).

[53] J. R. Yates, X. J. Wang, D. Vanderbilt, and I. Souza, Phys. Rev. B **75**, 195121 (2007).

[54] C. G. Van de Walle and J. Neugebauer, J. Appl. Phys. **95**, 3851 (2004).

[55] J. Wang, Z. Q. Wang, H. Cho, M. J. Kim, T. K. Sham, and X. H. Sun, Nanoscale **7**, 1718 (2015).

[56] N. Berseneva, A. Gulans, A. V. Krasheninnikov, and R. M. Nieminen, Phys. Rev. B **87**, 035404 (2013).

[57] B. Huang and H. Lee, Phys. Rev. B **86**, 245406 (2012).

[58] R. F. Liu and C. Cheng, Phys. Rev. B **76**, 014405 (2007).

[59] C. Attaccalite, M. Bockstedte, A. Marini, A. Rubio, and L. Wirtz, Phys. Rev. B **83**, 144115 (2011).

[60] K. Suenaga, H. Kobayashi, and M. Koshino, Phys. Rev. Lett. **108**, 075501 (2012).

[61] A. V. Krasheninnikov and K. Nordlund, J. Appl. Phys. **107**, 071301 (2010).

[62] O. V. Yazyev and L. Helm, Phys. Rev. B **75**, 125408 (2007).

[63] I. Jimenez, W. M. Tong, D. K. Shuh, B. C. Holloway, M. A. Kelly, P. Pianetta, L. J. Terminello, and F. J. Himpsel, Appl. Phys. Lett. **74**, 2620 (1999).

[64] S. P. Huber, E. Gullikson, R. W. E. van de Kruijs, F. Bijkerk, and D. Prendergast, Phys. Rev. B **92**, 245310 (2015).

[65] F. Jelezko and J. Wrachtrup, Phys. Status Solidi A **203**, 3207 (2006).